Electronic Supplementary Material (ESI) for Lab on a Chip.

- Electronic Supplementary Information -

Engineering deformation-free plastic spiral inertial microfluidic system for CHO cell clarification in biomanufacturing

Hyungkook Jeon,[a] Taehong Kwon,[a] Junghyo Yoon,[a] and Jongyoon Han[a,b,c,*]

[a]Research Laboratory of Electronics, [b]Department of Electrical Engineering and Computer Science, and [c]Department of Biological Engineering, Massachusetts Institute of Technology (MIT), Cambridge, MA 02139, USA.

*To whom correspondence should be addressed. E-mail: jyhan@mit.edu

Table of Contents

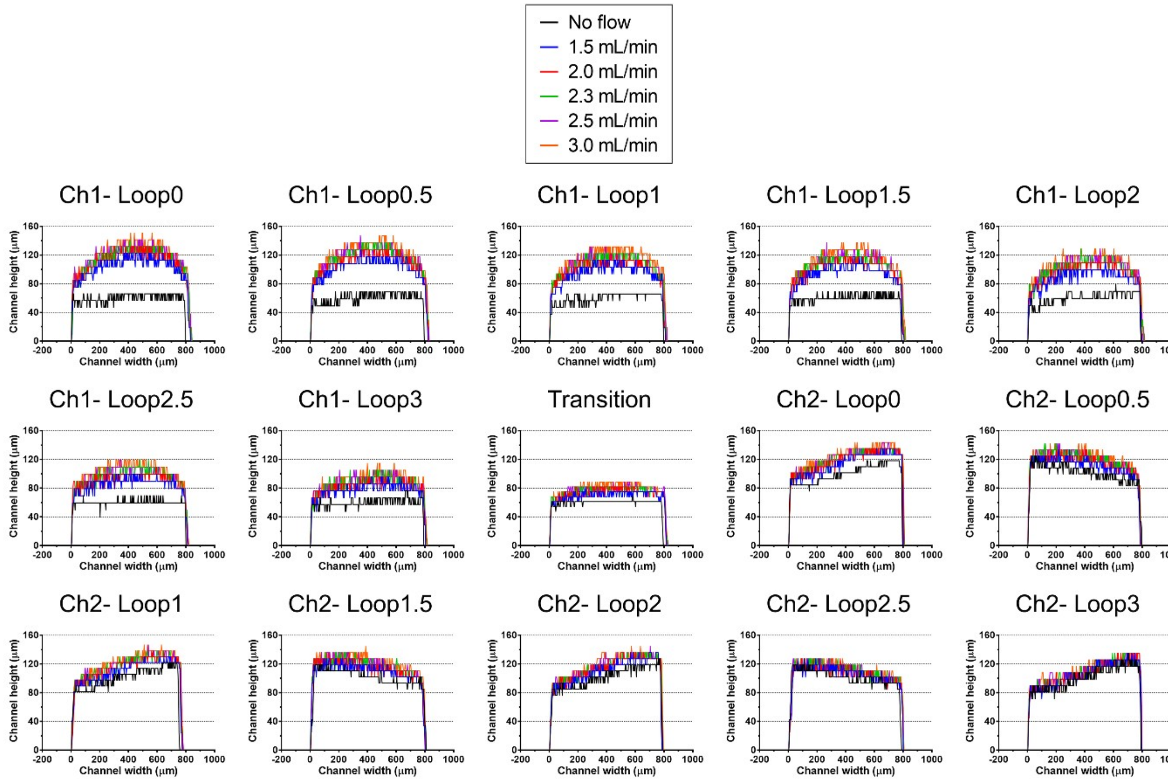

Fig. S1. Analysis of channel deformation in the MDDS device for blood separation based on the confocal imaging. Height profiles of the cross-section at each loop under various input flow rate conditions. MDDS device, multi-dimensional double spiral device.

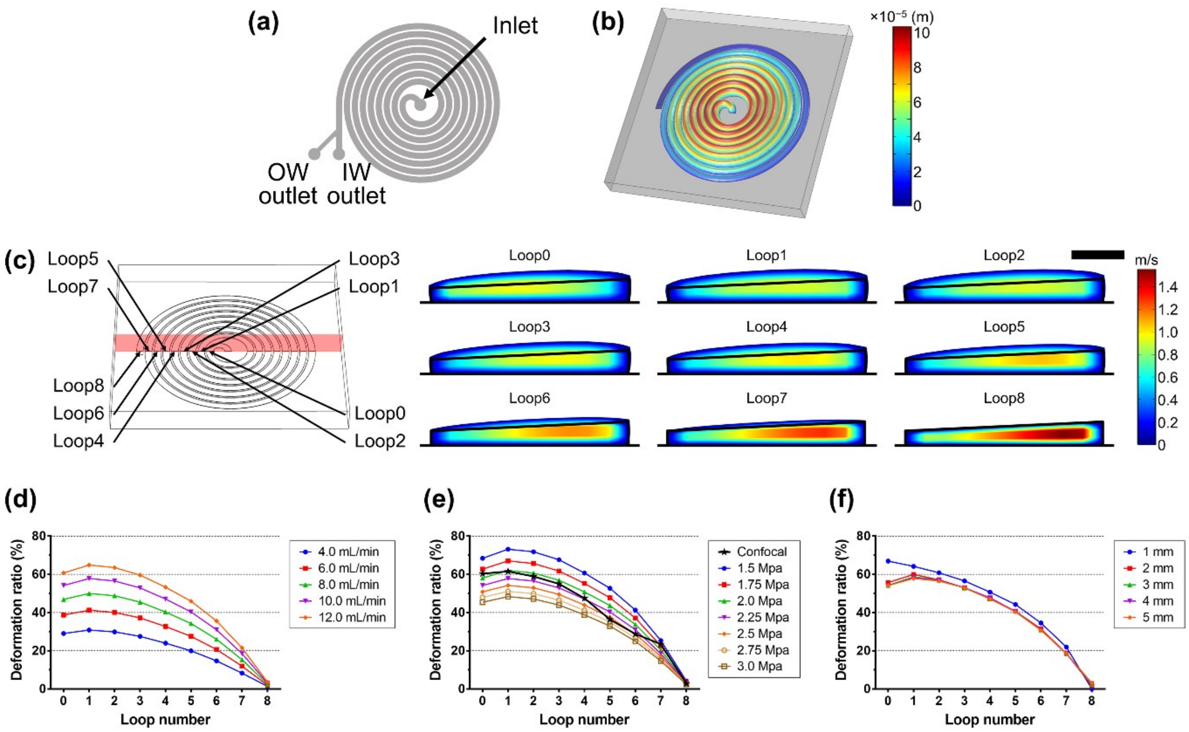

Fig. S2. Analysis of channel deformation in the PDMS spiral device for CHO cell retention based on numerical simulation. (a) Channel configuration of the CHO retention device. (b) A 3D profile of the overall channel deformation; for clearer visualization, the 3D deformation profile was amplified with a scale factor of 25. (c) The channel deformation at each loop in a cross-sectional view; the solid black line represents the initial channel outline (scale bar: 400 μm). Profiles of the deformation ratio at each loop under (d) various input flow rate conditions, (e) various Young's modulus conditions, and (f) various PDMS thickness conditions, obtained by the numerical simulation; in (e), the confocal imaging result at the optimal flow rate of 10 mL/min was overlaid for comparison. The deformation ratio was defined by '(change of the cross-section area)/(original cross-sectional area)'. All the numerical simulation results were obtained at default parametric conditions of the input flow rate (10 mL/min), Young's modulus (2.25 MPa), and PDMS thickness

(5 mm) except when the parameter becomes a variable. CHO cell, Chinese Hamster Ovary cell; IW, inner wall; OW, outer wall.

The channel deformation in the CHO retention device was also analyzed by the numerical simulation and confocal imaging methods. As shown in **Fig. S2**a, the second spiral device has a conventional single spiral configuration but has a specific dimension that was optimized for retention (or removal) of CHO cells in the size range of 10–20 μm. The device has a trapezoidal cross-section with 1,500 μm in width and 180 and 110 μm in height for the inner-and outer-wall sides, respectively, with eight loops.[1–3] The three parameters of 1) input flow rate (default: 10.0 mL/min), 2) Young's modulus of PDMS (default: 2.25 MPa), and 3) PDMS thickness (default: 5 mm) were modulated in the numerical simulation. **Fig. S2**b shows the overall channel deformation 3D profile of the device, and **Fig. S2**c shows the channel deformation at each loop in a cross-sectional view (the solid black line represents the initial channel outline), under the default conditions. Similar to the first device, the channel deformation was highest (~70% of deformation ratio from the initial dimension) at the inlet and decreased as going to the outlet according to the pressure decrease. **Fig. S2**d shows the profiles of the deformation ratio at each loop depending on the input flow rate. Due to the increased pressure drop, the deformation ratios for the entire channel regions increase as the input flow rate increases (total pressure drop in the entire channel: ~1.36 $\times 10^5$Pa, under the default parameter conditions). **Fig. S2**e shows the variation of the channel deformation profile depending on the PDMS modulus in the range of 1.5 to 3.0 MPa with the step size of 0.25 MPa. The results clearly showed that the deformation ratio significantly decreases as the modulus increases (up to 25% difference between 1.5 and 3.0 MPa conditions at the inlet region which has the highest deformation). In the simulation, the input flow is applied to the inlet surface as a boundary condition while the real input flow is infused into the device through an external tubing, so the inlet surface keeps its initial shape and dimension without deformation as shown in **Fig. S2**b. The constraint suppresses the channel deformation near the inlet region but becomes negligible as going away from the inlet. Due to the smaller applied pressure in the inlet region of the second spiral device compared to the first device, the suppression effect was more significant so that the deformation ratio at the channel of ‘loop0’ shows a lower value than the channel of ‘loop1’ (**Fig. S2**e). We also analyzed the channel deformation of the second spiral device depending on the PDMS thickness (**Fig. S2**f). Similar to the first device, the results represented that the effect of the PDMS thickness is negligible unless it becomes thin enough (<1 mm) to be comparable to the channel height.

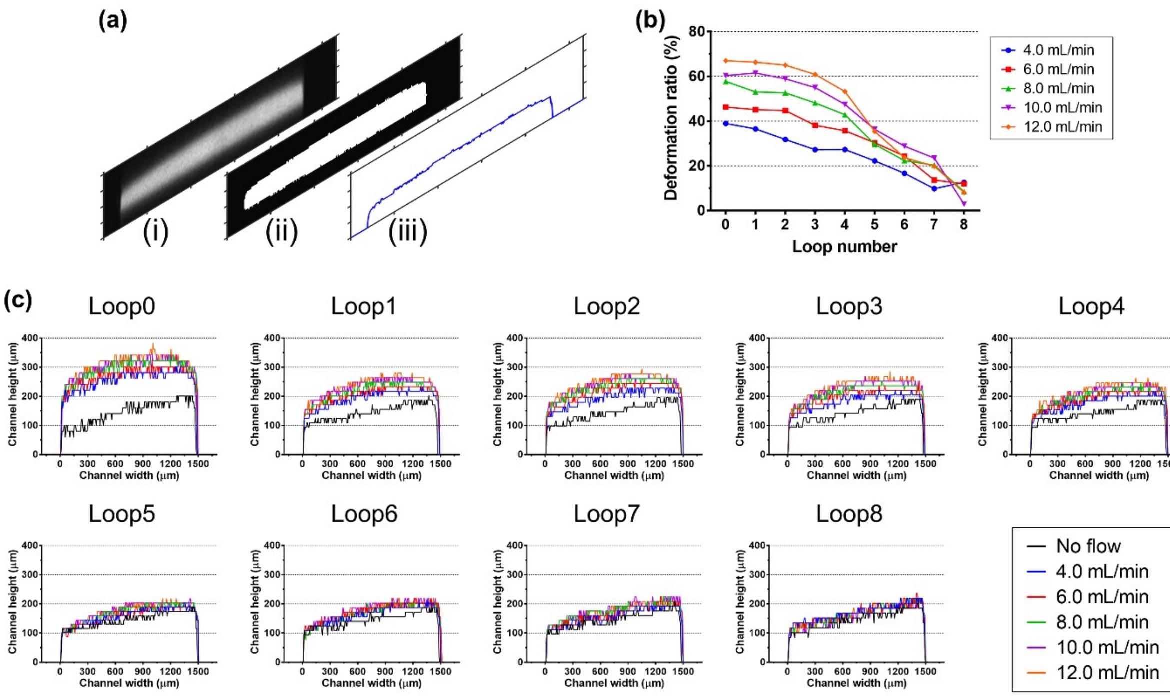

Fig. S3. Analysis of channel deformation in the PDMS spiral device for CHO cell retention based on the confocal imaging. (a) Conversion and analysis process of the confocal cross-sectional image at the inlet region of the device using a MATLAB code. (b) Profiles of the deformation ratio at each loop under various input flow rate conditions, where the deformation ratio was defined by '(change of the cross-section area)/(original cross-sectional area)'. (c) Height profiles of the cross-section at each loop under various input flow rate conditions. MDDS device, multi-dimensional double spiral device. CHO cell, Chinese Hamster Ovary cell.

Fig. S3a,c show the image conversion process and the height profiles at the cross-section of the inlet region of the second spiral device, respectively. Similar to the first spiral device, the confocal imaging results clearly showed the channel deformation from its original shape (represented by the solid black line) and increase of the deformation with increasing the input flow rate (**Fig. S3**c). **Fig. S3**b shows the profiles of the deformation ratio at each loop depending on the input flow rate. The profiles are very similar to the results from the numerical simulation (**Fig. S2**d) and clearly show the decrease of the deformation ratio as going from the inlet to the outlet and also the increase of the deformation ratio as increasing the input flow rate. Based on the comparison between the deformation profiles obtained from the numerical simulation and the confocal imaging in **Fig. S2**e, we found that the second spiral device showed also their best match at 2.25-MPa Young's modulus, which verifies that the same curing condition results in the same mechanical property of PDMS. From the numerical simulation result at Young's modulus of 2.25 MPa and the optimal flow rate of 10.0 mL/min, the average deformation ratio of the entire spiral channel in the MDDS device was 36.3%.

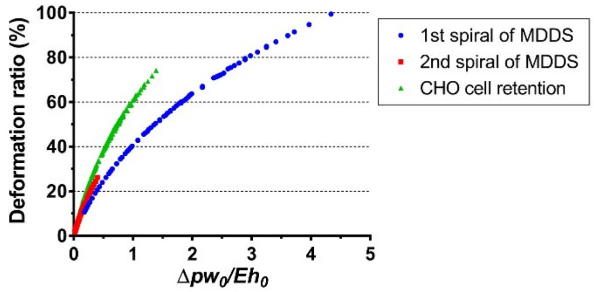

Fig. S4. The average deformation ratio of the MDDS and CHO cell retention devices depending on the theoretically calculated dimensionless number ($\Delta pw_0 / Eh_0$, where Δp represents the pressure drop applied to the device which was calculated by ignoring channel deformation, w_0 and h_0 denote the original channel width and height, respectively, and E means Young's modulus).

One can theoretically calculate the dimensionless number ($\Delta pw_0 / Eh_0$) to access the channel deformation. The following equations were used to calculate the hydraulic resistance and the pressure drop applied to the PDMS spiral devices:

$$\Delta p = R \times Q \tag{S1}$$

$$R = \frac{1}{1-0.63(h/w)} \frac{12\mu L}{h^3 w} \tag{S2}$$

where Δp, R, and Q denote the pressure drop, hydraulic resistance, and flow rate, respectively, and h, w, and L are height, width, and length of the channel, respectively, and μ represents dynamic viscosity of a fluid. From the equation (S2), the calculated hydraulic resistances for the 1st and 2nd spiral channels in the MDDS device for blood separation were 13.5 and 3.01 $\times 10^{12}$Pa·s/m^3, respectively, and the resistance for the CHO retention device was 1.21 $\times 10^{12}$Pa·s/m^3; the average height value was applied for the channel having a trapezoidal cross-section. **Fig. S4** shows the relationship between the deformation ratio ($\sim\Delta h / h_0$, obtained by the numerical simulation) and the dimensionless number ($\Delta p w_0 / E h_0$, theoretically calculated) for the two PDMS spiral devices. Here, the average deformation ratio over the entire channel region was used for $\Delta h / h_0$ while the median pressure value ($(p_{inlet} + p_{outlet}) / 2$) was used for Δp. In the case of the 1st spiral channel in the MDDS device, ($\Delta p_{1\mathrm{st\,spiral}} / 2 + \Delta p_{2\mathrm{nd\,spiral}}$) was applied as the median pressure value. Similar to **Fig. 2**l, for the MDDS device for blood separation, all the combinations of 12 flow rate conditions (from 0.25 to 3.0 mL/min with the step size of 0.25 mL/min) and 7 Young's modulus conditions (from 1.5 to 3.0 MPa with the step size of 0.25 MPa) were tested, resulting in a total of 84 conditions, and for the CHO retention device, all the combinations of 20 flow rate conditions (from 1.0 to 20.0 mL/min with the step size of 1.0 mL/min) and 7 Young's modulus conditions (from 1.5 to 3.0 MPa with the step size of 0.25 MPa) were tested, resulting in a total of 140 conditions. As shown in **Fig. S4**, the deformation ratio does not show linear dependency on the dimensionless number ($\Delta p w_0 / E h_0$), different from **Fig. 2**l. Because the theoretically calculated pressure drop does not reflect the channel deformation, it has a higher value than its actual value under the channel deformation, and the difference between the calculated and actual values increases as the dimensionless number ($\Delta p w_0 / E h_0$) increases due to a larger channel deformation. As a result, the deformation ratio has a nonlinear dependency on the dimensionless number ($\Delta p w_0 / E h_0$) with a decreasing slope.

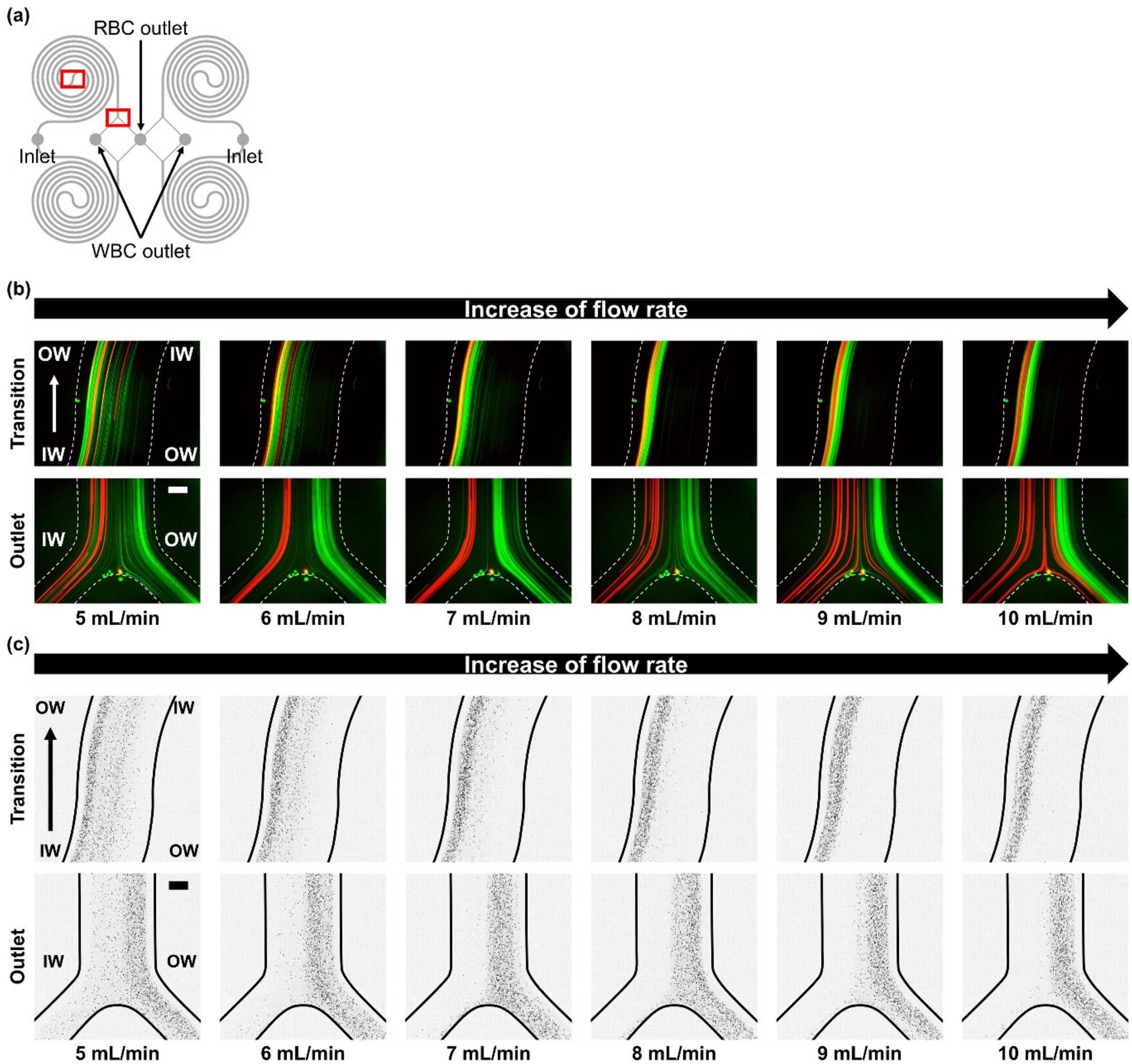

Fig. S5. Particle trajectories in the plastic MDDS device. (a) Channel configuration of the plastic MDDS device; the red boxes represent the observation spots. (b) Particle trajectories at the S-shaped transition region and the outlet bifurcation region under various input flow rate conditions; particles having diameters of 6 (green) and 10 μm (red) were used to mimic the movement of RBCs and WBCs, respectively (scale bar: 200 μm). (c) Trajectories of blood cells (500× diluted blood sample) at the S-shaped transition region and the outlet bifurcation region under various input flow rate conditions (scale bar: 200 μm). MDDS device, multi-dimensional double spiral device; IW, inner wall; OW, outer wall; RBC, red blood cell; WBC, white blood cell.

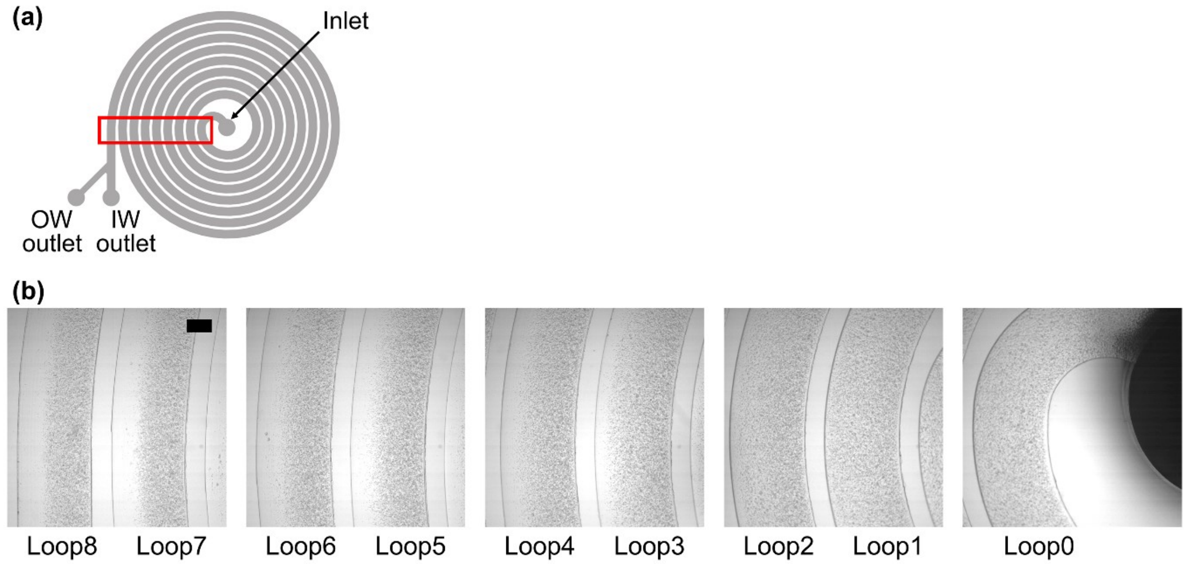

Fig. S6. Trajectories of CHO cells in the original PDMS spiral device for CHO cell retention. (a) Channel configuration of the original PDMS spiral device; the red box represents the observation spot. (b) Trajectories of CHO cells at each loop (scale bar: 500 μm). CHO cell, Chinese Hamster Ovary cell; IW, inner wall; OW, outer wall.

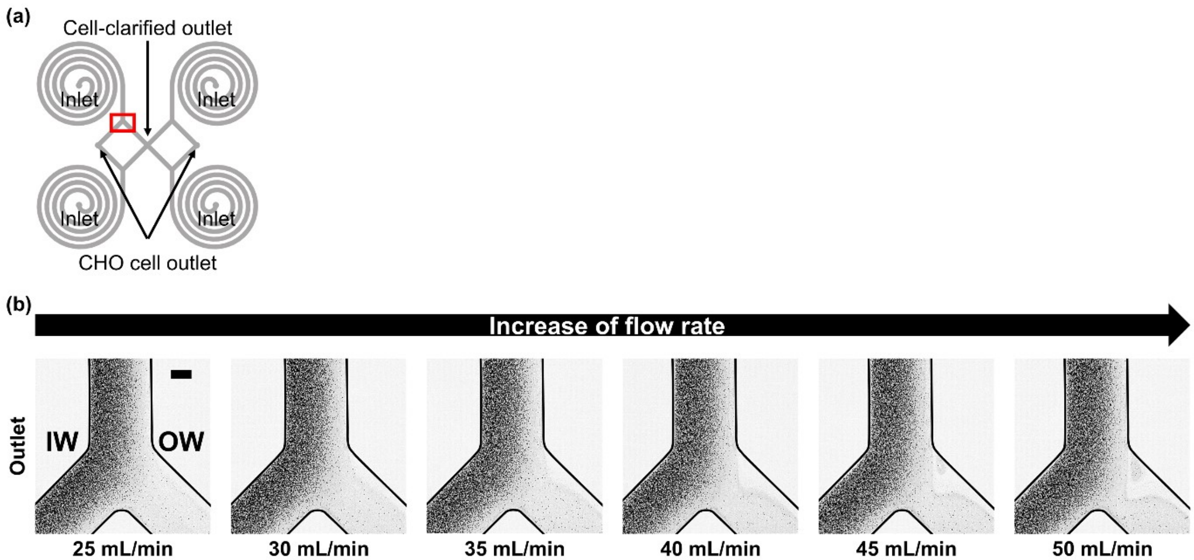

Fig. S7. Trajectories of CHO cells in the plastic spiral device for CHO cell retention. (a) Channel configuration of the plastic spiral device; the red box represents the observation spot. (b) Trajectories of CHO cells at the outlet bifurcation region under various input flow rate conditions (scale bar: 500 μm). CHO cell, Chinese Hamster Ovary cell; IW, inner wall; OW, outer wall.

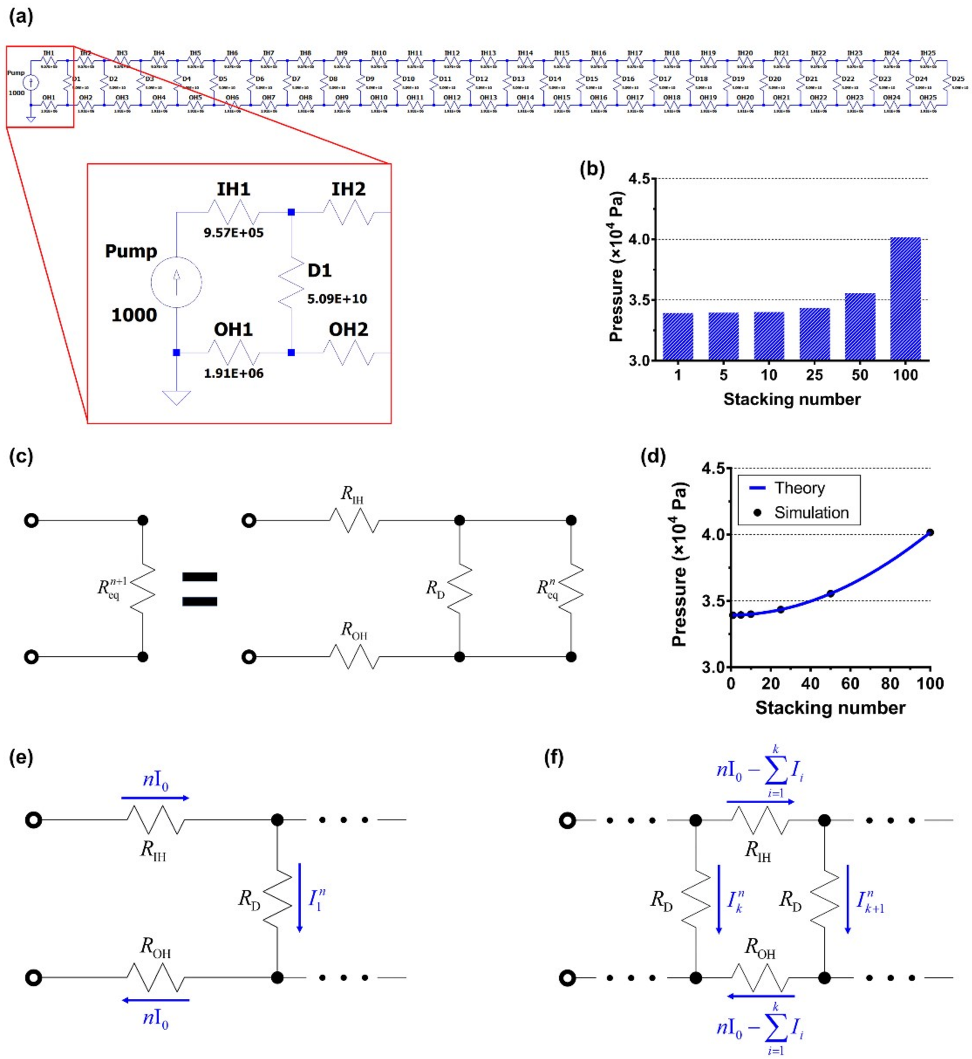

Fig. S8. Analysis of fluidic behavior in the multiplexed device based on electric circuit analogy. (a) The electric circuit model of the 25-layers-stacked device for circuit simulation. (b) The pressure (or voltage) drop applied to the multiplexed device depending on the stacking number, analyzed by circuit simulation. (c) The electric circuit model for theoretical calculation of the equivalent hydraulic resistance of the n -layers-stacked device (R_{eq}^{n}), where R_D , R_{IH} , and R_{OH} are hydraulic resistances of the spiral device and the inlet-holes and outlet-holes connection parts between layers, respectively. (d) Theoretical calculation (solid blue line) of the pressure (or voltage) drop applied to the multiplexed device depending on the stacking number, compared with the circuit simulation results (black circle). (e) The electric circuit model for theoretical calculation of the flow rate (or current) applied on the first-layer device. (f) The electric circuit model for the recurrence relation between flow rates into the k^{th}-layer and $(k+1)^{\text{th}}$-layer devices. IH, inlet holes; OH, outlet holes; D, device.

We analyzed fluidic behavior in the multi-layer stacked plastic spiral device based on the electric circuit analogy using circuit simulation and theoretical calculation, where hydraulic resistance, pressure, and flow rate can be interpreted by electrical resistance, voltage, and current, respectively.[4] The hydraulic resistance of the spiral channel was calculated based on the equation (S2) while the hydraulic resistance of the connection parts (inlet and outlet holes) were calculated based on the following equation because they have a circular cross-section:

$$R = \frac{128\mu L}{\pi d^4} \tag{S3}$$

where d and L are the diameter and length of the channel, respectively, and μ represents the dynamic viscosity of a fluid. One of the four spiral channels in the quad-version plastic CHO retention device has the following channel dimension: average height of 217.5 µm, width of 1,500 µm, and length of ~0.237 m. Based on the resistance equation for the channel having a rectangular cross-section, the calculated hydraulic resistance was ~2.03×10^{11} Pa·s/m^3. Because the plastic spiral device consists of four spiral channels, the hydraulic resistance of the quad-version plastic device (R_D) was calculated by diving the hydraulic resistance of a single device by four, resulting in R_D ~5.09×10^{10} Pa·s/m^3. The connection parts (inlet and outlet holes) have the following channel dimension: diameter of 2 mm and length of 1.5 mm. Based on the resistance equation for the channel having a circular cross-section, the calculated hydraulic resistance of a single hole was

~3.83 $\times 10^6$Pa·s/m^3. Because the quad-version plastic device has four inlets, the hydraulic resistance of inlet holes (R_{IH}) was calculated by dividing the hydraulic resistance of a single hole by four, resulting in R_{IH} ~9.57 $\times 10^5$Pa·s/m^3. The quad-version plastic device has three outlets (2 for the inner-wall side outlets and 1 for the outer-wall side outlet), but the majority of fluid comes from the two inner-wall side outlets by using an external flow regulator to harvest only the cell-clarified portion from the outer-wall side outlet. To simply the electric circuit model, we assumed that fluid comes out through only the two inner-wall side outlets at the same flow rate, so the hydraulic resistances of outlet holes (R_{OH}) were calculated by dividing the hydraulic resistance of a single hole by two, R_{OH} ~1.91 $\times 10^6$Pa·s/m^3.

An electric circuit simulation software (LTspice, Analog Devices, Inc., USA) was used for the electric circuit analogy. In modeling of the electric circuit, hydraulic resistance, pressure, and flow rate (40 mL/min × stacking number) were directly applied to electrical resistance, voltage, and current, respectively. For a more intuitive interpretation, a flow rate value having a ‘mL/min’ unit was directly applied to a current value of the pump. **Fig. S8**a shows the electric circuit model for the 25-layers-stacked device, where 25 device resistances (D#) are connected in parallel through the inlet hole resistances (IH#) and the outlet hole resistance (OH#). **Fig. 4**e shows profiles of the flow rate applied to each layer of a stacked device depending on the stacking number. **Fig. S8**b shows the pressure applied to the multiplexed device depending on the stacking number, which was calculated based on the voltage applied to the pump in the circuit simulation; (10^{-6}m^3/mL)×(1min/60s) was multiplied to the obtained voltage value for the unit change. As expected, the result shows that the applied pressure increases as the stacking number increases because more connection parts are engaged in the stacked device.

To obtain the closed-form formula of the hydraulic resistance and flow distribution in the multiplexed device, theoretical analysis was also performed based on the electric circuit analogy. As shown in **Fig. S8**c, from the equivalent circuit models, we can obtain the following recurrence relation between the hydraulic resistances of the n-layers-stacked device (R_{eq}^{n}) and the $(n+1)$-layers-stacked device (R_{eq}^{n+1}) as below:

$$\begin{aligned} R_{\mathrm{eq}}^{n+1} &= R_{\mathrm{IH}} + R_{\mathrm{OH}} + \left(\frac{1}{R_{\mathrm{D}}} + \frac{1}{R_{\mathrm{eq}}^{n}} \right)^{-1} \\ &= R_{\mathrm{C}} + \frac{R_{\mathrm{eq}}^{n} R_{\mathrm{D}}}{R_{\mathrm{eq}}^{n} + R_{\mathrm{D}}} \end{aligned} \qquad \text{(S4)}$$

where R_{D} and $R_{\mathrm{C}}(= R_{\mathrm{IH}} + R_{\mathrm{OH}})$ are hydraulic resistances of the spiral device and the (inlet-holes and outlet-holes) connection parts between layers, respectively. Using the arithmetics of determinants,[5] we can obtain the closed-form expression of the hydraulic resistances of the n-layers-stacked device (R_{eq}^{n}) as follows:

$$R_{\mathrm{eq}}^{n} = \frac{R_{\mathrm{c}}}{2} \times \frac{(\sqrt{1+4\beta}+1)^{2n+1} + (\sqrt{1+4\beta}-1)^{2n+1}}{(\sqrt{1+4\beta}+1)^{2n} - (\sqrt{1+4\beta}-1)^{2n}} \qquad \text{(S5)}$$

where $\beta(= R_{\mathrm{D}} / R_{\mathrm{C}})$ denotes the ratio between resistances of the device (R_{D}) and the connection-part (R_{C}). Also, using Ohm's law, we can calculate the pressure applied to the multiplexed device as follows:

$$V_{\mathrm{T}}^{n} = I_{\mathrm{T}}^{n} R_{\mathrm{eq}}^{n} = n\mathrm{I}_0 R_{\mathrm{eq}}^{n} = \frac{n\mathrm{I}_0 R_{\mathrm{c}}}{2} \times \frac{(\sqrt{1+4\beta}+1)^{2n+1} + (\sqrt{1+4\beta}-1)^{2n+1}}{(\sqrt{1+4\beta}+1)^{2n} - (\sqrt{1+4\beta}-1)^{2n}} \qquad \text{(S6)}$$

where I_0 is the desired flow rate for a single device, and V_{T}^{n} and $I_{\mathrm{T}}^{n}(= n\mathrm{I}_0)$ denote the pressure and the input flow rate applied to the n-layers-stacked device; note that $(10^{-6}\mathrm{m}^3/\mathrm{mL})\times(1\mathrm{min}/60\mathrm{s})$

should be multiplied to the obtained V_{T}^{n} value for compensation of using the unit of 'mL/min'. As shown in **Fig. S8**d, the theoretically calculated pressure was perfectly identical to the circuit simulation results at the tested conditions. To obtain the formula for the flow rate into an individual layer, we obtained the recurrence relation between flow rates into the k th-layer and $(k+1)$ th-layer devices based on the electric circuit models in **Fig. S8**e,f, as follows:

$$V_{\mathrm{T}}^{n} = n\mathrm{I}_{0} \times R_{\mathrm{IH}} + I_{1}^{n} \times R_{\mathrm{D}} + n\mathrm{I}_{0} \times R_{\mathrm{OH}} \tag{S7}$$

$$I_{1}^{n} = \frac{(V_{\mathrm{T}}^{n} - n\mathrm{I}_{0} R_{\mathrm{C}})}{R_{\mathrm{D}}} \tag{S8}$$

$$\left(n\mathrm{I}_{0} - \sum_{i=1}^{k} I_{i} \right) \times R_{\mathrm{IH}} + I_{k+1}^{n} \times R_{\mathrm{D}} + \left(n\mathrm{I}_{0} - \sum_{i=1}^{k} I_{i} \right) \times R_{\mathrm{OH}} - I_{k}^{n} \times R_{\mathrm{D}} = 0 \tag{S9}$$

$$I_{k+1}^{n} = I_{k}^{n} - \frac{1}{\beta}\left(n\mathrm{I}_{0} - \sum_{i=1}^{k} I_{i} \right) \tag{S10}$$

where I_{k}^{n} denotes the flow rate into the k th-layer device in the n -layers-stacked device. From the initial condition and the recurrence relation in the equations (S8) and (S10), we can obtain the closed-form expression of I_{k}^{n} as below:

$$\begin{aligned} I_{k}^{n} &= \frac{I_{\mathrm{T}}^{n}}{\beta^{k} 2^{2k-1}} \times \frac{(\sqrt{1+4\beta}+1)^{2n}(\sqrt{1+4\beta}-1)^{2k-1} + (\sqrt{1+4\beta}-1)^{2n}(\sqrt{1+4\beta}+1)^{2k-1}}{(\sqrt{1+4\beta}+1)^{2n} - (\sqrt{1+4\beta}-1)^{2n}} \\ &= \frac{n\mathrm{I}_{0}}{\beta^{k} 2^{2k-1}} \times \frac{(\sqrt{1+4\beta}+1)^{2n}(\sqrt{1+4\beta}-1)^{2k-1} + (\sqrt{1+4\beta}-1)^{2n}(\sqrt{1+4\beta}+1)^{2k-1}}{(\sqrt{1+4\beta}+1)^{2n} - (\sqrt{1+4\beta}-1)^{2n}} \end{aligned} \tag{S11}$$

As shown in **Fig. 4**e, we found that the results from the circuit simulation and the theoretical calculation for the flow rate were perfectly identical to each other, and the results showed that the flow rate variation increased as the stacking number increased due to the more connection parts engaged in the multiplexed device.

The first layer ($k=1$) has the maximum variation in flow rate from the desired flow rate for a single device (I_0). From the equation (S11), we derived a formula representing the maximum variation in flow rate as follows:

$$\begin{aligned}\nu &= \frac{I_1^n-\mathrm{I}_0}{\mathrm{I}_0}=\frac{n}{2\beta}\times\left(\frac{(\sqrt{1+4\beta}+1)^{2n}(\sqrt{1+4\beta}-1)+(\sqrt{1+4\beta}-1)^{2n}(\sqrt{1+4\beta}+1)}{(\sqrt{1+4\beta}+1)^{2n}-(\sqrt{1+4\beta}-1)^{2n}}\right)-1\\ &=2n\times\left(\frac{(\sqrt{1+4\beta}+1)^{2n-1}+(\sqrt{1+4\beta}-1)^{2n-1}}{(\sqrt{1+4\beta}+1)^{2n}-(\sqrt{1+4\beta}-1)^{2n}}\right)-1\end{aligned}\tag{S12}$$

In the equation (S12), the bracket approaches a constant value as $n\to\infty$ as follows:

$$\begin{aligned}&\lim_{n\to\infty}\left(\frac{(\sqrt{1+4\beta}+1)^{2n-1}+(\sqrt{1+4\beta}-1)^{2n-1}}{(\sqrt{1+4\beta}+1)^{2n}-(\sqrt{1+4\beta}-1)^{2n}}\right)\\ &=\lim_{n\to\infty}\left(\frac{(\sqrt{1+4\beta}+1)^{-1}+(\frac{\sqrt{1+4\beta}-1}{\sqrt{1+4\beta}+1})^{2n-1}(\sqrt{1+4\beta}+1)^{-1}}{1-(\frac{\sqrt{1+4\beta}-1}{\sqrt{1+4\beta}+1})^{2n}}\right)\\ &=\frac{1}{\sqrt{1+4\beta}+1}\end{aligned}\tag{S13}$$

Therefore, combining the equations (S12) and (S13), the maximum variation in flow rate, ν, diverges to infinity as $n\to\infty$. On the other hand, the maximum variation in flow rate, ν, converges to 0 as $\beta\to\infty$ as follows:

$$\begin{aligned}\lim_{\beta\to\infty}\nu &=\lim_{\beta\to\infty}\left(2n\times\left(\frac{(\sqrt{1+4\beta}+1)^{2n-1}+(\sqrt{1+4\beta}-1)^{2n-1}}{(\sqrt{1+4\beta}+1)^{2n}-(\sqrt{1+4\beta}-1)^{2n}}\right)-1\right)\\ &=\lim_{x\to\infty}\left(2n\times\left(\frac{x^{2n-1}+(x-2)^{2n-1}}{x^{2n}-(x-2)^{2n}}\right)-1\right),\ where\ x=\sqrt{1+4\beta}+1\\ &=\lim_{x\to\infty}\left(2n\times\left(\frac{2x^{2n-1}+\mathrm{L}}{-2n(-2)x^{2n-1}+\mathrm{L}}\right)-1\right)\\ &=2n\times\frac{1}{2n}-1=0\end{aligned}\tag{S14}$$

References

1 T. Kwon, H. Prentice, J. De Oliveira, N. Madziva, M. E. Warkiani, J.-F. F. P. Hamel and J. Han, *Sci. Rep.*, 2017, **7**, 6703.
2 T. Kwon, R. Yao, J. F. P. Hamel and J. Han, *Lab Chip*, 2018, **18**, 2826–2837.
3 T. Kwon, S. H. Ko, J. F. P. Hamel and J. Han, *Anal. Chem.*, 2020, **92**, 5267–5275.
4 K. W. Oh, K. Lee, B. Ahn and E. P. Furlani, *Lab Chip*, 2012, **12**, 515–545.
5 M. Kagan and X. Wang, 2015, 1–10.